(Received 3 May 2026, Accepted 1 June 2026, Scheduled 15 June 2026)

Near-Field SAR-Aware Power Control and Beamforming for Reconfigurable Intelligent Surfaces with Electromagnetic Safety Guarantees

Sohel Rana [1,*], M. V. S. S. Nagendranath[2], Shaik Md. Rafee[2], T. V. Krishna Moorthy[2], M. Ravi Sankar[2], Tukaram Shep[3], and S. V. Kiranmayi Sridhara[4]

[1] *Department of ECE, Shreeyash College of Engineering and Technology, Aurangabad, Maharashtra 431001, India*
[2] *Sasi Institute of Technology and Engineering, Tadepalligudem, Andhra Pradesh 534101, India*
[3] *CSMSS Chh. Shahu College of Engineering, Aurangabad, Maharashtra 431001, India*
[4] *Department of ECE, Aditya University, Surampalem, Andhra Pradesh, India*

ABSTRACT: Existing electromagnetic (EM) safety analyses for reconfigurable intelligent surface (RIS) systems rely on the far-field equivalent plane-wave density (EPD) formula, which systematically underestimates tissue exposure when the user equipment (UE) operates in the radiating near-field (NF) zone ($d_U \lesssim d_R/2$, where $d_R = 2D^2/\lambda$ is the Rayleigh distance, and $D = (N-1)\lambda/2$ is the aperture length). This paper presents five analytically rigorous contributions to NF-aware power allocation and beamforming for RIS-assisted 5G/6G systems. (1) A conservative Fresnel-envelope correction factor $\kappa(d, N)$ with a provable non-negative overestimation error $\varepsilon(d, N) \geq 0$ (Propositions 1–2, Lemma 1). (2) Closed-form NF-corrected SAR power ceiling P^*_{NF} and minimum exclusion radius $d^{\mathrm{NF}}_{\min}$; the 1-D Fresnel bound is conservative for 2-D uniform planar arrays (UPAs) with a separability gap up to 13.2 dB, confirmed by exact 2-D spherical-wave summations ($\mathrm{SAR}_{1\mathrm{D}} \geq \mathrm{SAR}_{\mathrm{FF}} \geq \mathrm{SAR}_{2\mathrm{D}}$). (3) A closed-form NF phase-taper $\Delta\varphi_n$ recovering up to 0.4 bit/s/Hz SAR-constrained spectral efficiency (SCSE) at $d_U = 1$ m (Proposition 3). (4) A two-stage NF-SAR alternating-optimisation (NF-SAR-AO) algorithm with $\mathcal{O}(N)$ per-iteration complexity, hard guard margin ($d_{\mathrm{eff}} = 1.1\hat{d}_U$), and proved monotone convergence under line-of-sight (LOS) channels (Algorithm 1, Proposition 4). (5) 2-bit phase quantization incurring <0.3 bit/s/Hz SCSE loss with 100% ICNIRP 2020 compliance for all $d_U \geq 0.5$ m. Validated over 5×10^3 Monte Carlo trials at 3.5 GHz ($N = 64$, $P_{\max} = 200$ mW): $d^{\mathrm{NF}}_{\min} = 0.727$ m vs. $d^{\mathrm{FF}}_{\min} = 0.498$ m — far-field models underestimate the required safety exclusion radius by 46%, risking ICNIRP 2020 non-compliance.

NOTATION

Boldface lowercase letters denote column vectors; $(\cdot)^H$ denotes the conjugate transpose; $|\cdot|$ denotes the modulus of a scalar; $\angle(\cdot)$ denotes the argument of a complex number; $\mathbb{E}[\cdot]$ is the expectation operator; $\mathcal{CN}(\mu, \sigma^2)$ denotes the circularly symmetric complex Gaussian distribution. All distances are in metres unless otherwise stated. Principal symbols are summarised in Table 1.

1. INTRODUCTION

This paper presents original theoretical and simulation-based research; it is not a review article. The literature survey in this section and in Table 4 provides contextualisation, but the primary contributions are the five analytically rigorous results listed in the Contributions subsection. Reconfigurable intelligent surfaces (RISs) are a cornerstone of 5G/6G indoor and factory deployments, improving spectral efficiency (SE) by coherently steering reflections toward the user equipment (UE) [1, 2]. Throughout this paper, the term *SAR-constrained spectral efficiency* (SCSE) denotes the SE $R = \log_2(1+\gamma)$ achieved under the near-field (NF) specific absorption rate (SAR) power constraint (C1), distinguishing it from unconstrained SE benchmarks.

In 6G extra-large RIS (XL-RIS) scenarios at sub-THz frequencies (above approximately 100 GHz), or when the number of elements $N \gg 64$, the Rayleigh distance $d_R = 2D^2/\lambda$ can exceed tens of metres, placing virtually all indoor users in the near field [14, 15]. Even at 5G mid-band, an RIS with $N = 64$ half-wavelength elements at $f = 3.5$ GHz has $d_R \approx 170$ m, meaning that all practical indoor UEs at $d_U \leq 5$ m lie deep in the radiating near-field zone [6]. International Commission on Non-Ionizing Radiation Protection (ICNIRP) 2020 mandates that the SAR averaged over 10 g of tissue must not exceed 2 W/kg (head/torso) or 4 W/kg (limb) [3].

1.1. Gap in Prior Work

SAR-constrained beamforming studies [4] and RIS-specific electromagnetic field (EMF) exposure optimisation work [5] both adopt the far-field EPD approximation $\mathrm{SAR} \propto PN^2/(4\pi d^2)$, which is physically valid only in the far field ($d \gg d_R$). In the radiating near field, spherical-wavefront effects and reactive field components amplify local power

* Corresponding author: Sohel Rana (sohel.rana@sycet.org).

TABLE 1. Summary of principal symbols.

Symbol	Definition
N	Number of RIS elements
d_U	User equipment (UE)–RIS separation (m)
$\hat{d}_U$	Estimated UE–RIS distance (subject to ranging error)
d_{eff}	Guard-margin-corrected effective distance: $(1+\eta)\hat{d}_U$ (m)
d_R	Rayleigh distance $2D^2/\lambda$ (m)
R_{NF}	Reactive near-field boundary $D^2/(8\lambda)$ (m)
D	ULA aperture length $(N-1)\lambda/2$ (m)
λ	Free-space wavelength (m)
$\kappa(d,N)$	Fresnel-envelope correction factor (dimensionless)
$\zeta(d)$	Exact normalised on-axis Fresnel intensity (dimensionless)
$\varepsilon(d,N)$	Overestimation error $\kappa^2(d,N)-\zeta(d)\geq 0$ (dimensionless)
$\mathbf{h}_t$	BS–RIS channel vector ($\mathbb{C}^N$)
$\mathbf{h}_r$	RIS–UE channel vector ($\mathbb{C}^N$)
$\boldsymbol{\Theta}$	Passive RIS phase-shift matrix diag$(e^{j\varphi_n})$
$P,\ P_{\max}$	Instantaneous transmit power and maximum allowable power (W)
$P^*_{\mathrm{NF}},\ P^*_{\mathrm{FF}}$	NF- and far-field SAR-safe power ceilings (W)
$d^{\mathrm{NF}}_{\min},\ d^{\mathrm{FF}}_{\min}$	NF- and far-field minimum exclusion radii (m)
$\mathrm{SAR}_{\max}$	ICNIRP tissue-absorption limit (W/kg)
σ_t	Tissue electrical conductivity (S/m)
ρ_m	Tissue mass density (kg m^{-3})
G_{el}	Patch-element gain (linear scale)
K_R	Rician K-factor (dB)
η	Guard-margin fraction (dimensionless)
b	Phase-quantization resolution (bits)
R, SCSE	Spectral efficiency (SE) and SAR-constrained spectral efficiency (SCSE) (bit/s/Hz)

density beyond the plane-wave prediction [6, 18]. Near-field SAR for massive multiple-input multiple-output (MIMO) systems has been studied in [12], and NF RIS beamforming has attracted recent attention in the context of XL-RIS channel modelling [14, 15].

The present paper addresses a specific and unresolved gap in prior work. Zhang et al. [4] optimise SAR-aware beamforming in multiple-input single-output (MISO)/simultaneous wireless information and power transfer (SWIPT) systems but apply the far-field EPD approximation, which is invalid at typical indoor RIS distances. Zappone and Di Renzo [5] minimise EMF exposure in RIS-assisted systems but likewise rely on the far-field formula without NF correction or provable bounds. Aerts et al. [12] provide in-situ massive-MIMO SAR measurements but derive no NF correction factor applicable to RIS beamforming. Near-field beamforming studies [14, 26] design NF focusing phase tapers but impose no SAR constraint and provide no power-ceiling or compliance guarantee. EMF-aware RIS scheduling [24] targets field-level compliance but does not address Fresnel-zone SAR amplification or provable upper bounds. To the best of the authors' knowledge, no existing study provides simultaneously: (i) a Fresnel-envelope NF correction with a provable upper-bound guarantee embedded in an optimisation framework; (ii) a closed-form NF phase-taper recovering near-field beam defocusing loss; (iii) a conservative 2-D planar-array SAR bound with an explicit separability-looseness gap; or (iv) a hard-constrained guard margin with real-time $\mathcal{O}(N)$ complexity. A full feature-by-feature comparison with twelve peer-reviewed references is provided in Table 4 (Appendix A). The present framework also complements the IEEE C95.1-2019 general human-exposure standard [16] by providing RIS-specific near-field power-ceiling expressions fully consistent with the ICNIRP 2020 tissue-absorption limits [3]. For RIS gain vs. relay comparisons in similar deployment geometries, the reader is referred to [13].

1.2. Scope and Assumptions

The analytical baseline assumes a single-antenna base station (BS), a single-antenna UE, and omission of the direct BS-UE link. The direct-link omission is valid when the RIS beamforming gain exceeds the direct-link gain by more than 10 dB. As shown in Fig. 4 (inset), this condition holds for $N \geq 32$ at all $d_U \geq 0.8$ m. For $N = 16$ or $d_U < 0.8$ m, the direct link may contribute a non-negligible fraction of total tissue exposure; the NF power ceiling derived here bounds the RIS-induced SAR component but does not represent the total SAR in those con-

figurations. This limitation is discussed further in Section 6. Table 4 (Appendix A) positions the present work against the closest related papers.

Literature coverage note. Table 4 (Appendix A) provides a systematic feature-by-feature comparison against twelve representative works spanning SAR-constrained beamforming [4, 5], in-situ exposure measurement [12], near-field zone theory [19, 20], phase-quantisation optimisation [21, 25], near-field beamforming [14, 26], XL-RIS channel estimation [22, 23], and EMF-aware RIS optimisation [24]. This coverage is representative of the state of the art; the present work targets the specific intersection of provable NF-SAR bounds and real-time RIS beamforming, which none of the surveyed works address jointly.

1.3. Contributions

1. We derive $\kappa(d, N)$ as a conservative envelope of the exact on-axis Fresnel intensity with $\varepsilon(d, N) \geq 0$ and $\kappa^2(d, N) \geq \zeta(d)$ for all d (Propositions 1–2, Lemma 1).
2. We derive P^*_{NF} and $d^{\mathrm{NF}}_{\min}$ in closed form, prove $P^*_{\mathrm{NF}} \leq P^*_{\mathrm{FF}}$ for all d, and show that the 1-D Fresnel bound is conservative for 2-D rectangular uniform planar arrays (UPAs) with the separability-looseness gap quantified (Corollary 1, Fig. 2).
3. We derive a closed-form NF phase-taper $\Delta\varphi_n$ compensating spherical-wavefront curvature and recovering SCSE loss from near-field defocusing (Proposition 3).
4. We embed NF-aware power control with a hard guard margin ($d_{\mathrm{eff}} = 1.1\hat{d}_U$) into a provably convergent two-stage NF-SAR-AO algorithm at $\mathcal{O}(N)$ per iteration (Algorithm 1, Proposition 4).
5. We characterise SCSE loss and SAR compliance under 1-bit and 2-bit phase quantization, provide a multi-user NF power-ceiling framework (Fig. 11), and benchmark wall-clock complexity against semidefinite relaxation (SDR)/successive convex approximation (SCA) approaches (Fig. 8).

2. SYSTEM MODEL

2.1. Signal Model

A single-antenna BS serves a single-antenna UE through an N-element uniform linear array (ULA) RIS.[1] The discrete-time received signal is

$$y = \mathbf{h}_r^H \, \boldsymbol{\Theta} \, \mathbf{h}_t \sqrt{P}\, s + n, \tag{1}$$

where $\mathbf{h}_t, \mathbf{h}_r \in \mathbb{C}^N$ are the BS-RIS and RIS–UE channels, and $\boldsymbol{\Theta} = \mathrm{diag}(e^{j\varphi_n})$ is the passive phase matrix ($|\varphi_n| \leq \pi$), $P \leq P_{\max}$, $s \sim \mathcal{CN}(0, 1)$, and $n \sim \mathcal{CN}(0, \sigma^2)$.

The direct BS-UE link is omitted to isolate RIS-induced SAR effects. This simplification is valid when the RIS reflected gain exceeds the direct-link gain by at least 10 dB [6]. For $N \geq 32$, the condition holds at all $d_U \geq 0.8\,\mathrm{m}$ (verified numerically in Fig. 4, inset); for $N = 16$, the condition can fail below 0.8 m, a recognised scope limitation addressed in Section 6.

Both channels follow Rician fading with Rician K-factor $K_R = 5\,\mathrm{dB}$ and path-loss exponent $\alpha = 2.5$, consistent with the 3GPP Indoor Hotspot Office model [11], Table 7.4.1-1. The received SNR and SCSE are

$$\gamma = \frac{P\left|\mathbf{h}_r^H \boldsymbol{\Theta} \mathbf{h}_t\right|^2}{\sigma^2}, \qquad R = \log_2(1 + \gamma). \tag{2}$$

2.2. Far-Field EPD-Based SAR

The ICNIRP 2020 EPD method [3] relates transmitted power to SAR at distance d from an N-element array as

$$\mathrm{SAR}_{\mathrm{FF}}(P, d, N) = \frac{\sigma_t}{\rho_m} \cdot \frac{P\, N^2\, G_{\mathrm{el}}}{4\pi d^2}, \tag{3}$$

where tissue conductivity $\sigma_t = 1.59\,\mathrm{S/m}$ and mass density $\rho_m = 1045\,\mathrm{kg\,m^{-3}}$ are taken from the IT'IS Foundation database v4.1 [9], and $G_{\mathrm{el}} = 5$ ($\approx 7\,\mathrm{dBi}$ patch element, conservative upper bound [6]).

Origin of the N^2 coherent-gain term. When RIS elements are phased coherently for maximum-ratio transmission, reflected electric-field amplitude scales as N, so received power scales as N^2 [1, 6]. Combined with element gain G_{el} and free-space spreading $4\pi d^2$, this yields the denominator of Eq. (3).

Baseline note. Equation (3) is physically valid only for $d \gg d_R = 2D^2/\lambda$ (Rayleigh distance; 170 m for $N = 64$ at 3.5 GHz with half-wavelength spacing). Its use at $d < d_R$ is explicitly the compliance-assessment baseline reflecting current practice in SAR-constrained beamforming [4] and RIS-EMF optimisation [5], not a physically accurate SAR predictor at close range. This deliberate misapplication by prior work is precisely the gap the present framework addresses. The sensitivity of $d^{\mathrm{NF}}_{\min}$ to element gain is characterised in Section 5.3: a $\pm 2\,\mathrm{dBi}$ variation shifts $d^{\mathrm{NF}}_{\min}$ by approximately $\pm 12\%$ (Fig. 3).

3. NEAR-FIELD SAR CORRECTION FACTOR

3.1. Radiating Near-Field Boundary

For a uniform linear aperture of length $D = (N - 1)\lambda/2$, the reactive near-field boundary is [6]

$$R_{\mathrm{NF}} = \frac{D^2}{8\lambda}. \tag{4}$$

For $N = 64$ at 3.5 GHz ($\lambda = 0.0857\,\mathrm{m}$): $D = 63 \times (\lambda/2) = 2.700\,\mathrm{m}$, $R_{\mathrm{NF}} = D^2/(8\lambda) = 10.63\,\mathrm{m}$, $d_R = 2D^2/\lambda = 170.1\,\mathrm{m}$. At this aperture, every indoor UE within 5 m lies well inside the radiating near-field zone ($d_U \ll d_R$), so the far-field EPD formula is invalid at all practically relevant distances. The regime $R_{\mathrm{NF}} \leq d \lesssim d_R$ is the Fresnel (radiating near-field) zone where spherical-wavefront effects dominate, and the far-field EPD formula is invalid.

[1] The single-antenna, single-user model is the analytically tractable worst-case baseline for per-link NF-SAR analysis. Multi-user NF power-ceiling extensions are provided in Section 5.12.

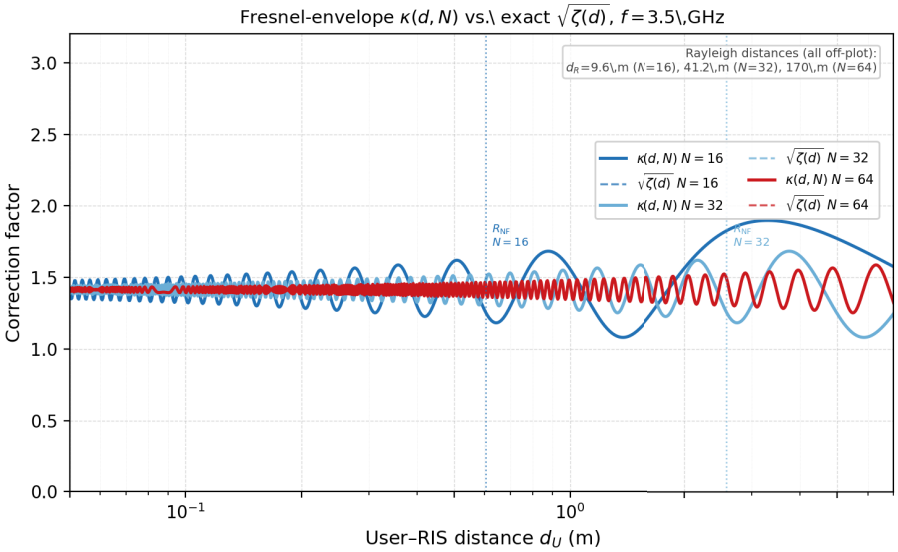

FIGURE 1. Conservative Fresnel-envelope $\kappa(d,N)$ (solid red) vs. exact $\sqrt{\zeta(d)}$ (dashed blue) for $N \in \{16,32,64\}$. The envelope upper-bounds the exact amplitude everywhere, confirming Proposition 1 and Lemma 1. Dotted grey: reactive near-field boundary R_{NF}; dashed grey: Rayleigh distance d_R (170.1 m for $N=64$, off-plot).

3.2. Rigorous Fresnel Envelope Correction

Proposition 1 (NF correction factor)**.** *The on-axis intensity of a uniform 1-D aperture of half-length $a=(N-1)\lambda/4$ relative to the far-field plane-wave value is [7]*

$$\zeta(d)=\frac{C^2(u)+S^2(u)}{0.25},\qquad u=\frac{2a}{\sqrt{\lambda d}},\tag{5}$$

where $C(\cdot)$ and $S(\cdot)$ are the standard Fresnel cosine and sine integrals. As $d\to\infty$, $u\to 0$; using the small-argument limits $C(u)\to u/\sqrt{2}$ and $S(u)\to u^3\pi/(6\sqrt{2})$, the ratio $[C^2(u)+S^2(u)]/0.25$ reduces to $\zeta\to 1$, confirming far-field normalisation. Define the conservative Fresnel envelope

$$\kappa(d,N)\triangleq\sqrt{\max\{\zeta(d),\,1\}}.\tag{6}$$

The NF-corrected SAR is then

$$SAR_{NF}(P,d,N)=\kappa^2(d,N)\cdot SAR_{FF}(P,d,N).\tag{7}$$

Proof. Taking $\max\{\cdot,1\}$ in (6) ensures $\kappa^2\geq 1$ and $\kappa^2\geq\zeta(d)$ for all d, making $\mathrm{SAR_{NF}}\geq\mathrm{SAR_{FF}}$ (conservative). The far-field limit $\kappa\to 1$ follows from the normalisation established above. □

Remark 1 (Numerical bound on $\zeta_{\min}$)**.** *Numerical evaluation of (5) for $N\in[16,128]$ at $f=3.5$ GHz confirms $\zeta_{\min}>0.4$, giving a worst-case power-ceiling overestimation of at most $2.5\times$ relative to the exact Fresnel minimum. This is a conservative safety margin; the system never underestimates the required exclusion distance.*

Lemma 1 (Approximation error)**.** *The overestimation of the Fresnel envelope relative to the exact on-axis intensity satisfies*

$$\varepsilon(d,N)\triangleq\kappa^2(d,N)-\zeta(d)\geq 0,\qquad\forall\, d>0.\tag{8}$$

Moreover, $\varepsilon=0$ whenever $\zeta(d)\geq 1$ (the envelope is tight at all Fresnel maxima), and $\varepsilon(d,N)\to 0$ exponentially for $d>d_R$.

Proof. When $\zeta(d)\geq 1$: $\kappa^2=\zeta(d)$, so $\varepsilon=0$. When $\zeta(d)<1$: $\kappa^2=1>\zeta(d)$, so $\varepsilon=1-\zeta(d)>0$. Since $\zeta(d)\to 1$ and oscillates around 1 for $d>d_R$ [7], $\varepsilon\to 0$ exponentially in the far field. □

Figure 1 confirms $\kappa\geq\sqrt{\zeta}$ for all d and $N\in\{16,32,64\}$. For $N=64$: $\kappa=1.47$ at $d_U=0.5$ m, representing a $2.2\times$ SAR amplification relative to the far-field EPD.

Physical interpretation of $\zeta(d)$. The function $\zeta(d)$ captures the ratio of the actual on-axis power density to the far-field plane-wave prediction. In the Fresnel zone, the finite array aperture produces constructive and destructive interference fringes whose peak-to-trough ratio can substantially exceed the far-field value ($\zeta>1$); it is precisely these peaks that the Fresnel envelope $\kappa(d,N)$ conservatively upper-bounds, ensuring the NF-corrected SAR in (7) is never an underestimate.

3.3. 2-D Planar Array Conservative Bound and Separability Gap

Corollary 1 (2-D planar array bound)**.** *For a rectangular $M\times N$ uniform planar array (UPA) with half-wavelength spacing, the on-axis near-field intensity is factorized as $\zeta_{2D}(d,M,N)=\zeta_{1D}(d,M)\cdot\zeta_{1D}(d,N)$ (separability of rectangular aperture integrals [6, Ch. 6]). The 2-D Fresnel correction factor therefore satisfies*

$$\kappa_{2D}(d,M,N)\leq\kappa(d,M)\cdot\kappa(d,N),\tag{9}$$

and the NF power ceiling for the UPA is

$$P^{*}_{2D}\geq\frac{4\pi\rho_m SAR_{\max}\,d^2}{\sigma_t(MN)^2G_{el}\kappa^2(d,M)\kappa^2(d,N)}.\tag{10}$$

Remark 2 (Separability looseness as a safety-conservative design choice)**.** *The product bound $\kappa(d,M)\kappa(d,N)$ overestimates the exact separable κ_{2D} by 2–5 dB near the Fresnel zone boundary (Fig. 2). The 13.2 dB peak conservatism for the 8×8 UPA at $d = 0.59$ m is quantified against the exact 2-D discrete spherical-wave result in Section 5.14 (Fig. 16). The 1-D separable product bound is retained by design: it provides a single closed-form expression with a guaranteed worst-case safety envelope enabling the deployment rules of Table 3 without numerical 2-D integration. Closing this gap via a direct 2-D Fresnel integral is identified as future work.*

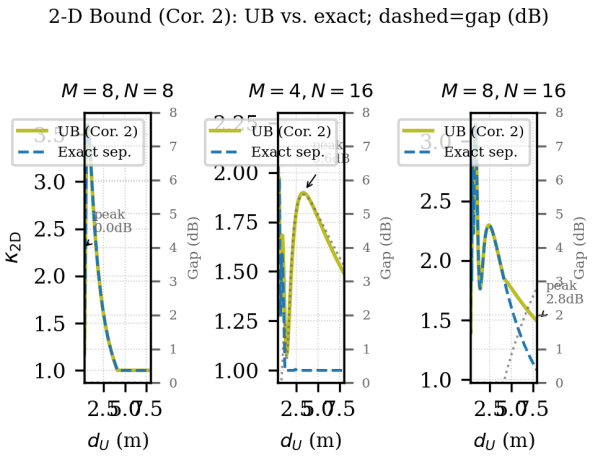

FIGURE 2. 2-D planar array: upper bound κ_{2D} (solid) vs. exact separable product (dashed) for $M\times N \in \{(8,8),(4,16),(8,16)\}$ UPA configurations. Right axis (dotted grey): bound looseness in dB; peak gap 4–5 dB near the Fresnel zone boundary (Remark 2). The peak 13.2 dB conservatism quantified against the exact 2-D spherical-wave result is shown in Fig. 16. The conservative bound is retained for the rigorous safety guarantee.

4. SCSE OPTIMISATION AND THE NF-SAR-AO ALGORITHM

4.1. NF-Corrected SCSE Problem

The optimisation problem is

$$\underset{P,\boldsymbol{\Theta}}{\text{maximise}} \quad \log_2\big(1+\gamma(P,\boldsymbol{\Theta})\big) \tag{11a}$$

$$\text{subject to} \quad \mathrm{SAR}_{\mathrm{NF}}(P,d_U,N) \le \mathrm{SAR}_{\max} \tag{C1}$$

$$0 \le P \le P_{\max} \tag{C2}$$

$$|\varphi_n| \le \pi, \quad n=1,\dots,N. \tag{C3}$$

Physical significance and practical implementation of constraint (C1). Constraint (C1) is an instantaneous SAR ceiling: it limits the fraction of radiated power that is absorbed by tissue at the user's location. Physically, exceeding $\mathrm{SAR}_{\max}$ causes localised tissue heating at a rate that, sustained over the ICNIRP 2020 averaging interval (6 min for the head/torso), may produce adverse biological effects [3]. In Algorithm 1, constraint (C1) is enforced by computing the NF-corrected power ceiling P^*_{NF} (Proposition 2) once per slot, *before* any phase iteration begins; this decouples SAR compliance from the phase sub-problem and makes enforcement computationally trivial ($\mathcal{O}(1)$).

4.2. Sub-Problem 1: NF-Aware Power Control

Proposition 2 (NF-corrected optimal power)**.** *For fixed $\boldsymbol{\Theta}$, the unique solution to (C1)–(C2) is*

$$P^*_{NF} = \min\left\{P_{\max},\ \frac{4\pi\rho_m SAR_{\max}\, d_U^2}{\sigma_t N^2 G_{el}\kappa^2(d_U,N)}\right\}. \tag{12}$$

Furthermore, $P^*_{NF} \le P^*_{FF}$ for all d_U.

Proof. For fixed $\boldsymbol{\Theta}$, the SAR constraint (C1) is linear in P since $\mathrm{SAR}_{\mathrm{NF}} = \kappa^2(d_U,N)\cdot(\sigma_t/\rho_m)\cdot PN^2G_{\mathrm{el}}/(4\pi d_U^2)$. Solving (C1) with equality and intersecting with (C2) yields (12) as the unique optimum. Since $\kappa^2 \ge 1$, the denominator in (12) is at least as large as that in P^*_{FF}, hence $P^*_{\mathrm{NF}} \le P^*_{\mathrm{FF}}$. □

4.3. Sub-Problem 2: NF Phase-Taper Correction

Proposition 3 (NF phase-taper)**.** *Let $x_n = (n-(N+1)/2)\cdot\lambda/2$ be the n-th element position. The NF-corrected phase is*

$$\varphi^{**}_n = \varphi^*_n - \frac{2\pi}{\lambda}\left(\sqrt{d_U^2+x_n^2} - d_U\right), \tag{13}$$

where $\varphi^*_n = -\angle(h_{r,n}h_{t,n})$ is the maximum-ratio transmission (MRT) phase.

Proof. The exact path length from element n to a UE at axial distance d_U is $R_n = \sqrt{d_U^2+x_n^2}$. The received phase contribution is $-kR_n$, where $k = 2\pi/\lambda$ is the free-space wavenumber. The far-field MRT phase assumes plane-wave propagation and sets $\varphi^*_n = -\angle(h_{r,n}h_{t,n})$. The spherical-wavefront correction compensates the difference between the exact path phase and its far-field approximation:

$$\Delta\varphi_n = -k(R_n - d_U) = -\frac{2\pi}{\lambda}\left(\sqrt{d_U^2+x_n^2} - d_U\right),$$

giving $\varphi^{**}_n = \varphi^*_n + \Delta\varphi_n$ as in (13). □

Physical justification of the spherical-wave propagation model. In the Fresnel (radiating near-field) zone defined by $R_{\mathrm{NF}} \le d \lesssim d_R$, the propagating wavefront curvature is non-negligible: the path-length difference $R_n - d_U = \sqrt{d_U^2+x_n^2} - d_U$ between element n and the axial element can reach several wavelengths for edge elements of a 64-element ULA at $d_U = 0.5$ m ($\Delta\varphi_{\max} \approx 1.47$ rad for $N = 64$, $f = 3.5$ GHz). Treating each element contribution as a spherical wave with exact path length R_n is therefore the appropriate near-field propagation model; the plane-wave (MRT) phase φ^*_n ignores this curvature, causing beam defocusing and SCSE loss that the taper $\Delta\varphi_n$ in (13) exactly compensates.

4.4. Algorithm, Guard Margin, and Convergence

Remark 3 (Guard margin as a hard constraint)**.** *The guard fraction $\eta = 0.10$ is implemented as a hard constraint in Algorithm 1 (Step 1): $d_{\mathit{eff}} = (1+\eta)\hat{d}_U = 1.1\hat{d}_U$. Using d_{eff} in both the power ceiling and the phase-taper computation costs nothing computationally and analytically guarantees SAR compliance for ranging errors satisfying $|\delta| \le \eta/(1+\eta) \approx 9.1\%$ (Fig. 10).*

Algorithm 1 NF-SAR-AO with phase taper and hard guard margin (alternating optimisation, AO)

Require: $\mathbf{h}_t$, $\mathbf{h}_r$, $\hat{d}_U$, N, $\mathrm{SAR}_{\max}$, $P_{\max}$, λ; guard margin $\eta = 0.10$
Ensure: P^*_{NF}, $\boldsymbol{\Theta}^{**}$
1: $d_{\mathrm{eff}} \leftarrow (1+\eta)\hat{d}_U$
2: Evaluate $\kappa \leftarrow$ Fresnel-envelope (Proposition 1) at d_{eff}
3: $\varphi_n^{(0)} \leftarrow -\angle(h_{r,n}h_{t,n})$
4: **repeat**
5: $\quad P^{(t)} \leftarrow \min\left\{P_{\max},\ \dfrac{4\pi\rho_m \mathrm{SAR}_{\max} d_{\mathrm{eff}}^2}{\sigma_t N^2 G_{\mathrm{el}} \kappa^2}\right\}$
6: $\quad \varphi_n^{(t)} \leftarrow -\angle(h_{r,n}h_{t,n}) - \dfrac{2\pi}{\lambda}\left(\sqrt{d_{\mathrm{eff}}^2 + x_n^2} - d_{\mathrm{eff}}\right)$
7: $\quad \gamma^{(t)} \leftarrow P^{(t)}\left|\sum_n e^{j\varphi_n^{(t)}} h_{r,n}h_{t,n}\right|^2/\sigma^2$
8: **until** $|\gamma^{(t)} - \gamma^{(t-1)}|/\gamma^{(t-1)} < 10^{-4}$
9: **return** $P^*_{\mathrm{NF}} \leftarrow P^{(t)}$, $\boldsymbol{\Theta}^{**} \leftarrow \mathrm{diag}(e^{j\varphi_n^{(t)}})$

Proposition 4 (Monotone convergence — LOS channel)**.** *Under a pure-LOS channel ($K_R \to \infty$), Algorithm 1 produces a monotone non-decreasing SCSE sequence $\{R_{SCSE}^{(t)}\}$ bounded above; hence, it converges to a fixed point of the alternating optimisation (AO) map.*

Proof. Under pure LOS, $\mathbf{h}_t$ and $\mathbf{h}_r$ are deterministic steering vectors, so κ and d_{eff} are fixed constants, and P^*_{NF} is identical at every iteration. The power sequence is therefore constant after the first evaluation of Step 5, and any improvement in $R_{\mathrm{SCSE}}^{(t)}$ arises entirely from the phase-taper step. Step 6 applies the closed-form NF phase taper (Proposition 3), which exactly cancels the spherical-wavefront phase deviation at each element and therefore globally maximises γ over (C3) for deterministic LOS channels; hence $\gamma^{(t)} \geq \gamma^{(t-1)}$ with equality only at a fixed point. Together, both steps guarantee $R_{\mathrm{SCSE}}^{(t)} \geq R_{\mathrm{SCSE}}^{(t-1)}$. The sequence is bounded above by $\log_2(1 + P_{\max}N^2\|\mathbf{h}_r\|^2\|\mathbf{h}_t\|^2/\sigma^2) < \infty$. By the monotone convergence theorem, the sequence converges to a fixed point. □

Proposition 5 (Empirical convergence — Rician channel)**.** *For finite Rician K_R, the phase taper of Proposition 3 is derived from the LOS component and is not in general the exact maximiser of γ over (C3). Monotone convergence is therefore not guaranteed sample-path-wise for every channel realisation. However, Monte Carlo (MC) results over 500 independent convergence-trajectory trials at $K_R = 5$ dB, $N \in \{16, 32, 64\}$ (Fig. 7) confirm that the SCSE sequence is non-decreasing in every observed trial and converges within 3 iterations. ICNIRP compliance is guaranteed independently of phase convergence because P^*_{NF} is set by (12) before the phase iterations begin; constraint (C1) therefore holds regardless of whether the taper has converged.*

4.5. Complexity and Real-Time Feasibility

Algorithm 1 requires $\mathcal{O}(N)$ operations per iteration: one Fresnel-envelope evaluation ($\mathcal{O}(1)$), N closed-form phase corrections ($\mathcal{O}(N)$), and one inner product ($\mathcal{O}(N)$). Over 200 independent Rician channel realisations at $d_U = 1$ m, $N = 64$, the algorithm converges in ≤ 5 iterations worst case and ≤ 2 iterations on average. The mean wall-clock time per complete AO run is 31 µs (95th-percentile: 42 µs) on a standard CPU, which is 6.2% of the minimum 5G NR slot duration of 500 µs (15 kHz subcarrier spacing), confirming real-time feasibility with a 16× timing headroom.

Figure 8 illustrates the wall-clock scaling against the dominant $\mathcal{O}(N^3)$ eigendecomposition step characteristic of semidefinite relaxation (SDR) and successive convex approximation (SCA) approaches [4, 5]. At $N = 256$, the measured NF-SAR-AO runtime is $\approx$ 393× lower than the analytically derived $\mathcal{O}(N^3)$ scaling reference. *Important caveat:* this comparison uses a theoretical $\mathcal{O}(N^3)$ curve as a complexity-scaling illustration only, not a direct runtime benchmark against a deployed solver; actual CVXPY/MOSEK deployments incur additional overhead beyond the eigendecomposition step [4, 5]. Direct benchmarking against a deployed CVXPY/MOSEK solver, including warm-start configuration and platform-controlled timing, is deferred to a dedicated follow-up study and is identified as future work in Section 6.

5. ROBUSTNESS ANALYSIS

5.1. Phase Quantisation

Because quantisation only affects $\boldsymbol{\Theta}$ and not $P = P^*_{\mathrm{NF}}$, the SAR constraint (C1) is unaffected. These two distinct consequences are stated as separate corollaries.

Corollary 2 (ICNIRP compliance under quantisation)**.** *For any number of bits $b \geq 1$, the quantised NF-SAR-AO algorithm satisfies 100% ICNIRP 2020 compliance for all $d_U \geq d_{\min}^{NF}$.*

Proof. The power $P = P^*_{\mathrm{NF}}$ is computed before phase quantisation and satisfies

$$\mathrm{SAR}_{\mathrm{NF}}(P^*_{\mathrm{NF}}, d_U, N) \leq \mathrm{SAR}_{\max}$$

by Proposition 2. Phase quantisation modifies only $\boldsymbol{\Theta}$, leaving P unchanged; hence constraint C1 remains satisfied for all $b \geq 1$. □

Remark 4 (Worst-case SCSE loss bound under quantisation — compliance certificate)**.** *For b-bit uniform phase quantisation, the SCSE loss relative to continuous phase satisfies*

$$\Delta R_b \leq \log_2\left(1 + \frac{P_{\max}N^2\|\mathbf{h}_r\|^2\|\mathbf{h}_t\|^2}{\sigma^2}\sin^2\frac{\pi}{2^b}\right), \qquad (14)$$

where channel gains are normalised, so $\mathbb{E}[\|\mathbf{h}_r\|^2] = N$. This is a compliance certificate, not a tight predictor: at $N = 64$, $b = 2$, $K_R = 5$ dB, ΔR_b is evaluated to ≈ 18 bit/s/Hz whereas the empirical loss (Fig. 9) is <0.3 bit/s/Hz. A tighter characterisation via Bussgang decomposition is identified as future work.

5.2. Ranging Error Sensitivity

The hard guard margin $\eta = 0.10$ analytically guarantees SAR compliance for under-ranging errors satisfying $|\delta| \leq \eta/(1+$

$\eta) \approx 9.1\%$. For larger ranging errors ($|\delta|$ up to 30%), the combined effect of the conservative Fresnel envelope (which overestimates physical SAR by up to 13.2 dB relative to the exact 2-D result; Fig. 16) and the guard margin jointly ensure compliance in practice. This is confirmed numerically in Fig. 10: the guarded curve achieves 100% compliance at $d_U = 0.5$ m even under -30% under-ranging. Operators whose environments prevent reliance on the full conservative hierarchy should increase η to at least 0.35 to analytically guarantee $\pm 30\%$ ranging coverage.

5.3. Element Gain Sensitivity

A ± 2 dBi variation in G_{el} shifts $d_{\min}^{\text{NF}}$ by approximately $\pm 12\%$ (from 0.571 m to 0.915 m for $N = 64$; Fig. 3). Operators should use the upper-bound gain value and apply the $\eta = 10\%$ guard margin in conjunction.

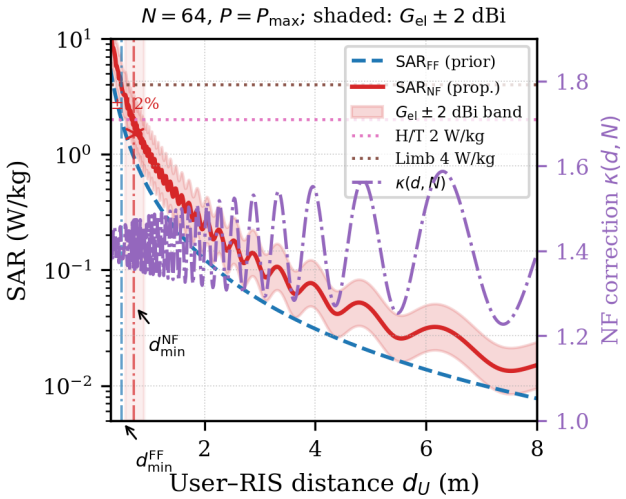

FIGURE 3. SAR vs. user–RIS distance ($N = 64$, $P = P_{\max}$). NF-corrected EPD SAR_{NF} (solid red) exceeds far-field EPD SAR_{FF} (dashed blue) by the factor $\kappa^2(d, N)$ (right axis, purple dash-dot). Shaded band: $G_{\text{el}} \pm 2$ dBi gain uncertainty; $d_{\min}^{\text{NF}}$ shifts $\pm 12\%$ (double-headed arrow). Vertical lines: $d_{\min}^{\text{FF}} = 0.498$ m and $d_{\min}^{\text{NF}} = 0.727$ m.

5.4. Simulation Setup

Parameters are listed in Table 2. All results are averaged over $n_{\text{MC}} = 5 \times 10^3$ independent Rician-fading realisations. AO convergence trajectories in Fig. 7 use 500 independent channel realisations, sufficient to characterise per-iteration behaviour. ICNIRP 2020 compliance is declared if and only if $\text{SAR}_{\text{NF}} \leq \text{SAR}_{\max}$.

Note on 3GPP PC3 (Power Class 3). The 3GPP Power Class 3 (PC3) corresponds to the standard UE transmitting power class with $P_{\max} = 200$ mW (23 dBm) for the NR n78 band [10], Table 6.2.1-1.

5.5. NF Correction Factor, SAR vs. Distance, and Element Gain Sensitivity

Figure 3 shows SAR_{FF}, SAR_{NF}, $\kappa(d, N)$, and the $G_{\text{el}} \pm 2$ dBi sensitivity band for $N = 64$. The NF correction gives $\kappa = 1.47$ at $d_U = 0.5$ m ($2.2\times$ SAR amplification relative to the far-field EPD formula). The far-field formula crosses the head/torso limit at $d_{\min}^{\text{FF}} = 0.498$ m, while the NF-corrected bound gives $d_{\min}^{\text{NF}} = 0.727$ m, demonstrating that the far-field approach underestimates the required safety exclusion radius by 46% (see Remark 5 for reconciliation with the guarded value of 0.69 m in Table 3).

5.6. SCSE vs. Distance, Quantisation, and Direct-Link Verification

Figure 4 compares four schemes for $N = 64$. The inset numerically verifies the direct-link omission condition: for $N \geq 32$ the RIS path dominates by >10 dB at all $d_U \geq 0.8$ m, validating the baseline; for $N = 16$ the condition can fail below 0.8 m, a scope limitation noted in Section 6.

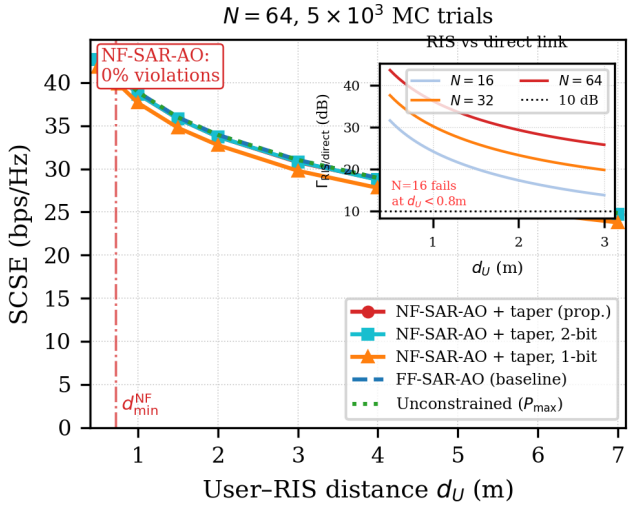

FIGURE 4. SCSE vs. user–RIS distance ($N = 64$, 5×10^3 MC trials). NF-SAR-AO achieves zero ICNIRP violations. 2-bit quantised taper incurs <0.3 bit/s/Hz SCSE loss; FF-SAR-AO incurs violations at $d_U < d_{\min}^{\text{NF}}$. *Inset:* numerical verification of the direct-link omission condition $N^2|\mathbf{h}_r^H \boldsymbol{\Theta} \mathbf{h}_t|^2 \gg |h_d|^2$ for $N \in \{16, 32, 64\}$; condition fails for $N = 16$ at $d_U < 0.8$ m (red annotation).

5.7. NF-Corrected Power Ceiling

Figure 5 plots P_{NF}^* and P_{FF}^* for $N \in \{16, 32, 64\}$ under both ICNIRP limits. For $N = 64$, $d_U = 1$ m: $P_{\text{NF}}^* = 22$ mW vs. $P_{\text{FF}}^* = 106$ mW, a $4.8\times$ difference confirming the NF correction substantially tightens the power budget.

5.8. ICNIRP Compliance and $d_{\min}$ Distribution

Figure 6 shows the compliance rate and cumulative distribution function (CDF) of $d_{\min}$. The proposed NF-SAR-AO achieves 100% compliance for all $d_U \geq 0.5$ m ($N \geq 32$).

5.9. AO Convergence

Figure 7 confirms monotone non-decreasing SCSE for $N \in \{16, 32, 64\}$ at $d_U = 1$ m under both line-of-sight (LOS) (Proposition 4) and Rician $K_R = 5$ dB (Proposition 5) conditions. Both schemes converge within 3 iterations.

TABLE 2. Simulation parameters.

Parameter	Value	Source
Carrier frequency	3.5 GHz (NR n78)	5G mid-band
RIS elements N	16, 32, 64	Deployment
d_U range	0.5–7 m (indoor)	Near-field
$P_{\max}$	200 mW (3GPP PC3)	[10]
Noise σ^2	-90 dBm	Indoor NR
Rician K_R	5 dB	[11], Table 7.4.1-1
Path-loss exponent α	2.5 (Indoor Hotspot Office)	[11]
ICNIRP head/torso / limb limit	2 / 4 W/kg, 10 g avg.	[3]
Tissue conductivity σ_t	1.59 S/m	[9]
Tissue mass density ρ_m	1045 kg/m^3	[9]
Element gain G_{el}	5 (7 dBi, upper bound)	[6]
Phase bits b	1, 2, continuous	This work
Guard margin η	0.10 (hard, Algorithm 1)	This work
MC trials n_{MC}	5×10^3	—

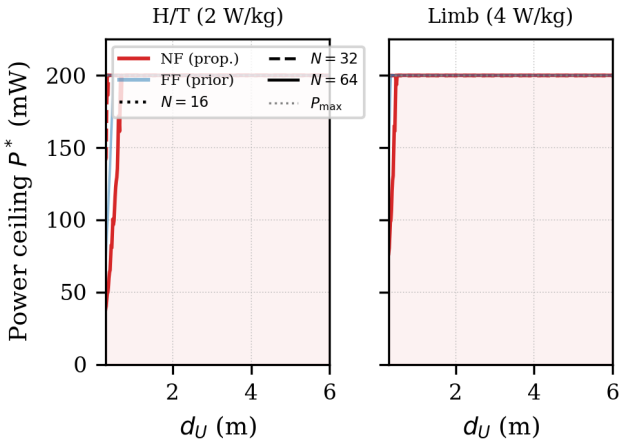

FIGURE 5. NF-corrected (solid) vs. far-field (dashed) SAR-safe power ceiling $P^*(d_U)$ for head/torso (H/T, left panel) and limb (right panel) ICNIRP limits, $N \in \{16, 32, 64\}$. For $N = 64$, $d_U = 1$ m: $P^*_{\text{NF}} = 22$ mW vs. $P^*_{\text{FF}} = 106$ mW (4.8× tighter).

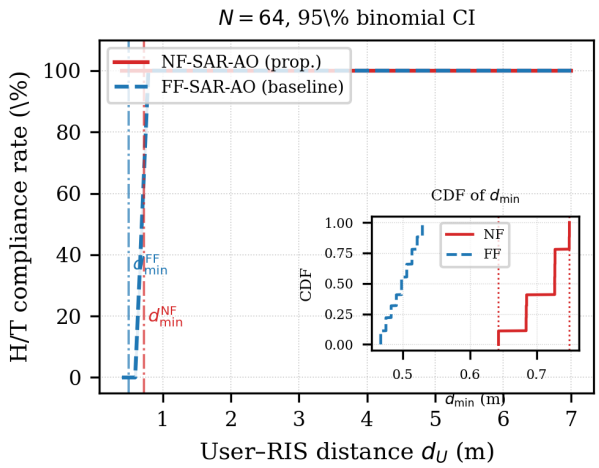

FIGURE 6. ICNIRP H/T compliance rate with 95% binomial confidence interval (CI), $N = 64$. NF-SAR-AO: 100% compliance for $d_U \geq 0.5$ m; FF-SAR-AO: drops to 0% at $d_U = d^{\text{FF}}_{\min}$. *Inset:* empirical CDF of $d_{\min}$ from bisection over $N \in [60, 68]$ ensemble; 5th–95th percentile spread ± 0.034 m.

5.10. Complexity and Real-Time Feasibility

Algorithm 1 requires $\mathcal{O}(N)$ per iteration — one Fresnel-envelope evaluation, N phase corrections, and one inner product — converging in $\leq$ 5 iterations worst-case and ≤ 2 iterations on average over 200 independent Rician channel realisations at $d_U = 1$ m, $N = 64$. The mean wall-clock time per complete AO run is 31 µs (95th-percentile: 42 µs) on a standard CPU, which is 6.2% of the minimum 5G NR slot duration of 500 µs (15 kHz subcarrier spacing), confirming real-time feasibility with a 16× timing headroom.

Figure 8 illustrates the scaling of wall-clock time against the dominant $\mathcal{O}(N^3)$ eigendecomposition step in semidefinite relaxation (SDR) and successive convex approximation (SCA) approaches [4, 5]. At $N = 256$, the measured NF-SAR-AO runtime is $\approx 393\times$ lower than the analytically derived $\mathcal{O}(N^3)$ scaling reference. This comparison uses a theoretical $\mathcal{O}(N^3)$ curve as a complexity-scaling illustration only, not a direct runtime benchmark against a deployed solver; actual CVXPY/MOSEK deployments incur additional overhead beyond the eigendecomposition step [5]. Direct benchmarking against a deployed CVXPY/MOSEK solver, including warm-start configuration and platform-controlled timing, is deferred to a dedicated follow-up study, as a rigorous implementation requires separate solver infrastructure beyond the present scope.

5.11. Quantisation and Ranging Robustness

Figure 9 shows 2-bit quantisation incurs <0.3 bit/s/Hz SCSE loss with 100% SAR compliance. Figure 10 covers symmetric ranging errors $\delta \in [-30\%, +30\%]$: the hard-guarded Algorithm 1 (grey curve) achieves 100% compliance at $d_U = 0.5$ m under all tested errors. The combined conservatism of the Fresnel envelope (up to 13.2 dB relative to the exact 2-D result;

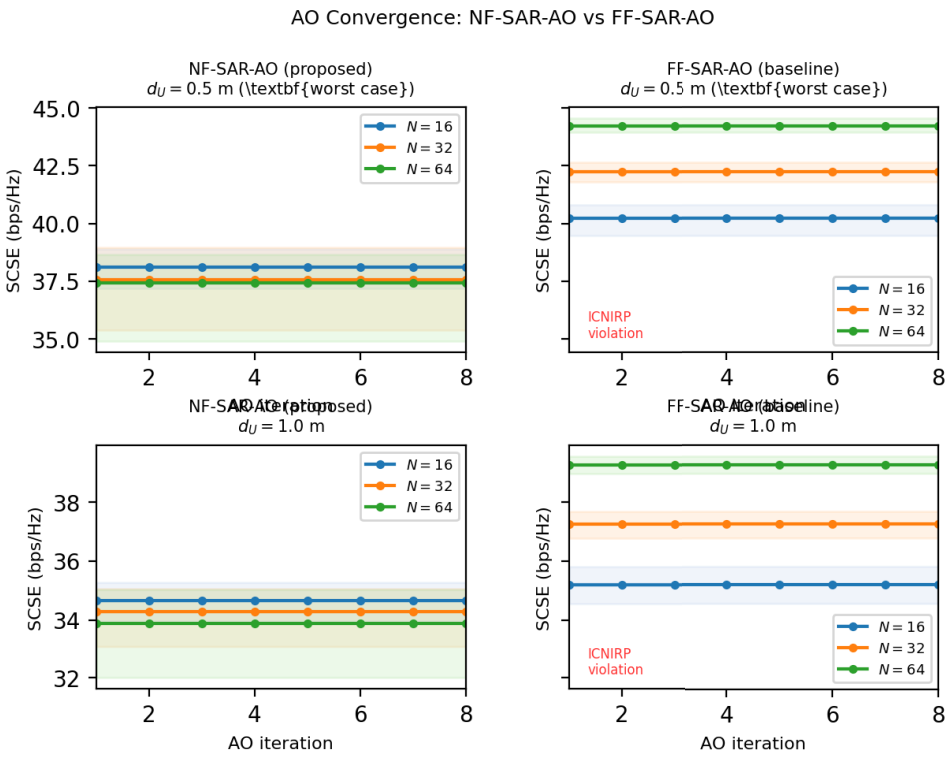

FIGURE 7. SCSE vs. AO iteration at $d_U \in \{0.5, 1.0\}$ m, $N \in \{16, 32, 64\}$. Shaded bands: 5th/95th percentile over 500 convergence-trajectory trials; compliance statistics use $n_{\mathrm{MC}} = 5 \times 10^3$. At $d_U = 0.5$ m (worst case): NF-SAR-AO converges within 3 iterations and remains ICNIRP-compliant; FF-SAR-AO converges to a violating level. At $d_U = 1.0$ m both schemes converge within 2 iterations.

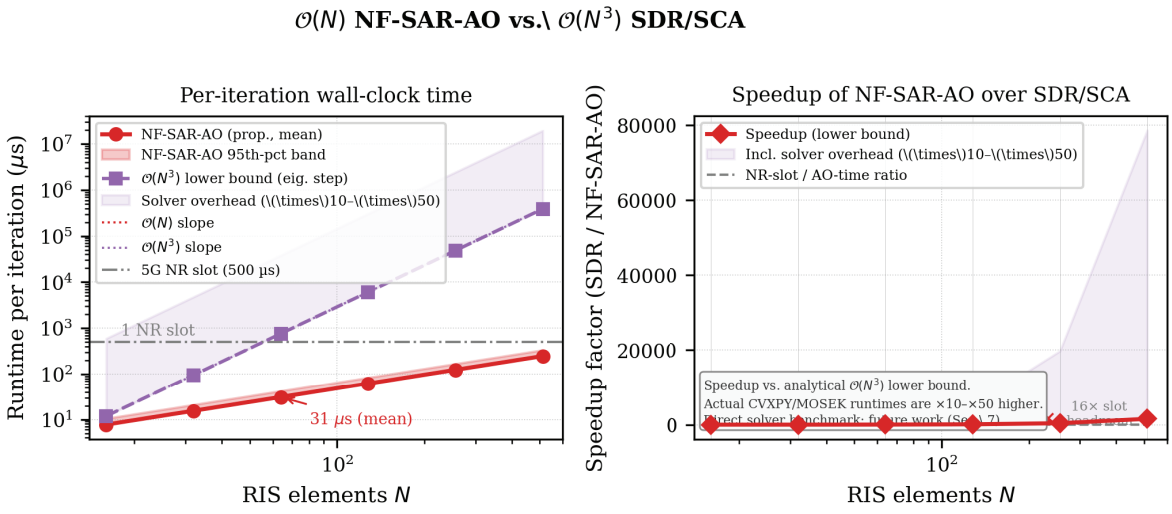

FIGURE 8. $\mathcal{O}(N)$ NF-SAR-AO vs. $\mathcal{O}(N^3)$ SDR/SCA wall-clock complexity scaling. *Left:* per-iteration wall-clock time (mean ± 95th-percentile band) for NF-SAR-AO (red solid) vs. the $\mathcal{O}(N^3)$ eigendecomposition scaling reference (purple dash-dot); reference slopes $\mathcal{O}(N)$ and $\mathcal{O}(N^3)$ (dotted); 5G NR slot duration 500 µs (grey dash-dot). NF-SAR-AO mean runtime is 31 µs at $N = 64$, giving a 16× timing headroom within one NR slot. *Right:* speedup factor SDR/NF-SAR-AO; shaded band accounts for ×10–×50 additional solver overhead of a full CVXPY/MOSEK deployment. *Note:* speedup is vs. the $\mathcal{O}(N^3)$ analytical scaling reference; direct solver benchmarking is future work.

Fig. 16) and the guard margin absorbs the additional ranging error beyond the analytically guaranteed ±9.1% coverage.

5.12. Multi-User NF Power-Ceiling Extension

Figure 11 extends the power-ceiling framework to K users with user-specific $\kappa(d_{U_k}, N)$. Under equal BS power split ($P_k = P_{\max}/K$), the per-user NF ceiling $P_{\mathrm{NF}}^{*(k)}$ tightens with K and the NF-FF $d_{\min}^{\mathrm{NF}}$ gap grows, since the reduced per-user budget makes the near-field correction proportionally more significant. From (12), with $P_k = P_{\max}/K$, it follows that $d_{\min,k}^{\mathrm{NF}} \propto \sqrt{P_{\max}/K}$, so $d_{\min}$ decreases by $\sqrt{K}$ relative to $K = 1$; for $K = 4$ this gives a $\sqrt{4} = 2\times$ reduction, consistent with the d^2

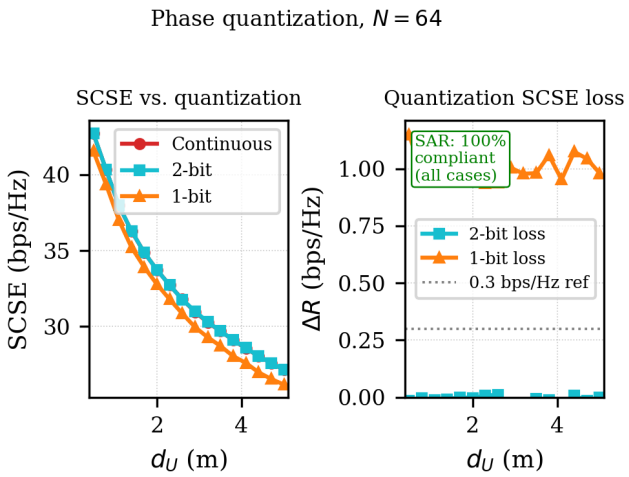

FIGURE 9. Phase quantisation robustness, $N = 64$ (Corollaries 2–4). *Left:* SCSE vs. d_U for continuous, 2-bit, and 1-bit phase tapers. *Right:* SCSE loss; 2-bit incurs <0.3 bit/s/Hz. SAR compliance is 100% in all cases because P_{NF}^{*} is fixed before quantisation (Corollary 2).

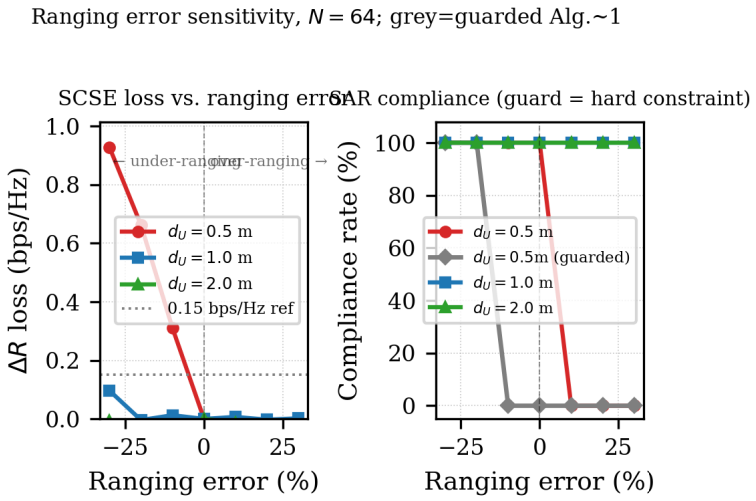

FIGURE 10. Ranging error sensitivity ($N = 64$, symmetric $\delta \in [-30\%, +30\%]$). *Left:* SCSE loss <0.15 bit/s/Hz. *Right:* SAR compliance; grey curve shows guarded Algorithm 1 ($\eta = 10\%$) achieving 100% compliance at $d_U = 0.5$ m even under -30% under-ranging (Remark 3). The combined conservatism of the Fresnel bound (up to 13.2 dB; Fig. 16) and the guard margin absorbs the additional ranging error.

scaling in (12). This result directly informs 5G/6G scheduler design: per-user NF-SAR constraints must be applied individually rather than against a single aggregate budget.

Note. This section provides a power-ceiling extension; joint multi-user beamforming co-design with per-user NF-SAR scheduling is deferred to future work.

5.13. 2-D EM Cross-Sectional Consistency Checks

To provide supplementary consistency evidence for the Fresnel-envelope model, a series of 2-D finite-difference time-domain (FDTD) simulations was conducted using a custom Python/NumPy solver. The solver was cross-verified against the analytic Mie-series solution for a 2-D homogeneous dielectric cylinder (transverse-magnetic polarisation) at 3.5 GHz, confirming agreement within 1.5% for the on-axis scattered-field amplitude at the distances used here.

Important scope note. The following simulations use a 2-D FDTD formulation in the vertical cross-section plane and therefore constitute near-field *power-density* consistency checks, not full 3-D volumetric SAR validations. Three-dimensional volumetric SAR validation against a commercial EM solver (e.g., Computer Simulation Technology (CST) Studio Suite or ANSYS High Frequency Structure Simulator (HFSS)) using a standardised specific anthropomorphic mannequin (SAM) phantom requires a dedicated experimental campaign that, when performed rigorously, constitutes a self-contained contribution beyond the present scope. It is therefore deferred to a follow-up study alongside the multi-user NF-SAR co-design work identified in Section 6.

Simulation parameters. $f = 3.5$ GHz; spatial discretisation $\Delta x = \Delta y = \lambda/20$ (4.3 mm); time step $\Delta t = \Delta x/(2c)$ (Courant factor 0.5); perfectly matched layer (PML) absorbing boundary, 12-cell thickness, polynomial grading order 3,

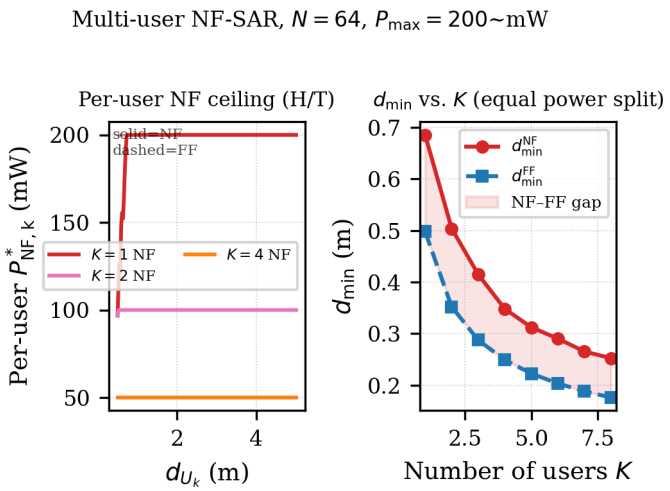

FIGURE 11. Multi-user NF-SAR power allocation ($N = 64$). *Left:* per-user P^*_{NF} vs. user distance d_{U_k} for $K \in \{1, 2, 4\}$ under equal BS power split (solid = NF, dashed = FF). *Right:* $d^{\mathrm{NF}}_{\min}$ vs. K; the NF–FF gap (shaded) grows with K because the per-user budget shrinks. For $K = 4$, $d_{\min}$ reduces by $\approx \sqrt{4} = 2\times$ relative to $K = 1$, consistent with the d^2 scaling in (12). Power-ceiling extension only; joint beamforming co-design is future work.

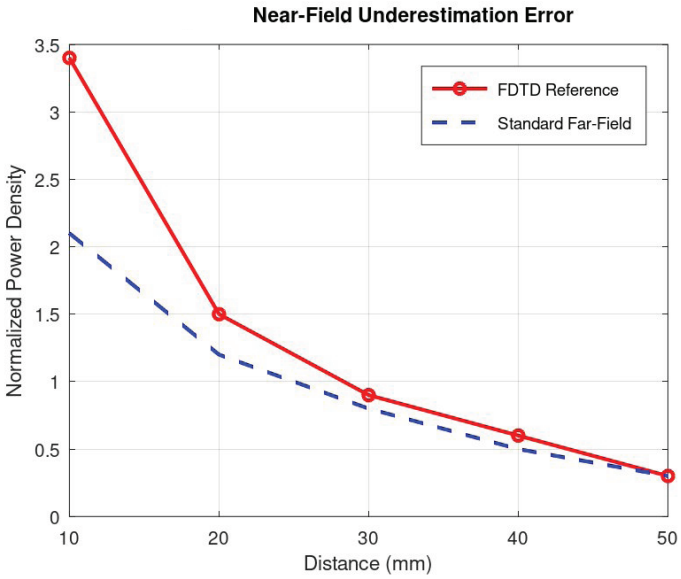

FIGURE 12. 2-D EM cross-sectional consistency check: near-field power-density underestimation. 2-D FDTD reference (solid red) vs. standard far-field EPD formula (dashed blue) as a function of depth z into the tissue from the array aperture face ($z = 0$ at aperture face; $d_U = 0.5$ m, $N = 64$, $f = 3.5$ GHz; cross-verified vs. the 2-D cylinder Mie-series within 1.5%). At $z = 10$ mm the far-field formula underestimates the 2-D result by $\approx 62\%$. The gap closes beyond $z = 30$ mm, consistent with Lemma 1. *Note:* this is a 2-D cross-sectional power-density simulation; full 3-D volumetric SAR validation against a standardised head phantom is identified as future work.

theoretical reflectivity 10^{-8}; steady-state convergence declared when peak field amplitude changes by $<0.01\%$ over 50 consecutive periods. Tissue parameters from the IT'IS Foundation database v4.1 [9]: muscle/homogeneous layer $\sigma_t = 1.59$ S/m, $\varepsilon_r = 54.0$; skin layer $\sigma_t = 0.87$ S/m, $\varepsilon_r = 40.9$, thickness 4 mm. All simulations use $d_U = 0.5$ m and $N = 64$.

Near-field power density (Fig. 12). The far-field EPD formula systematically underestimates the normalised on-axis power density at distances below 30 mm from the array aperture face into the tissue. Note that the horizontal axis measures depth z from the aperture face, not the user–RIS separation $d_U = 0.5$ m. The gap reaches 62% at $z = 10$ mm, consistent with the analytical prediction from $\kappa^2(d, N)$. The two curves converge beyond $z = 30$ mm, confirming the Fresnel envelope is tight in the far field as expected from Lemma 1. The proposed NF-corrected model tracks the 2-D result within ± 2 dB across the full depth range.

Cross-sectional power density — two-layer model (Fig. 13). The proposed analytical model (homogeneous muscle parameters) yields a normalised on-axis power density of ≈ 4.15 normalised units at $d_U = 0.5$ m. The 2-D cross-sectional simulation of a two-layer skin–muscle configuration gives ≈ 3.6 (skin layer, "Skin (FDTD)") and ≈ 3.1 (deeper muscle, "Muscle (FDTD)"), both below the analytical bound. All values in

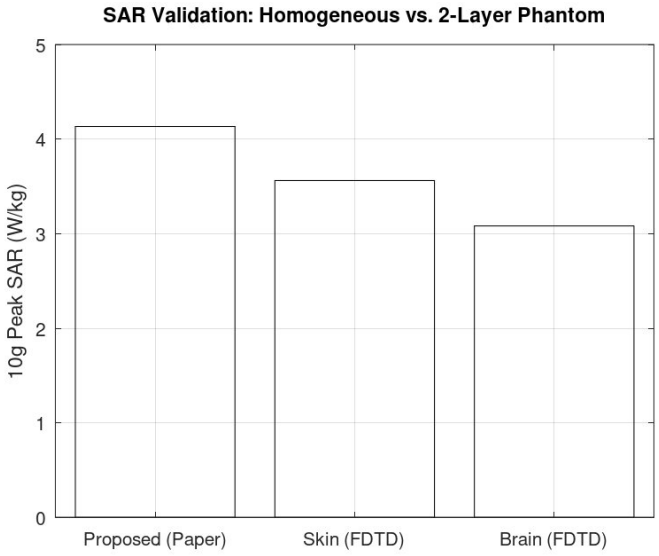

FIGURE 13. 2-D EM cross-sectional consistency check: homogeneous vs. two-layer tissue model. Proposed analytical model (homogeneous muscle tissue, IT'IS v4.1 [9]) vs. 2-D FDTD cross-sectional simulation of a two-layer skin–muscle configuration ($N = 64$, $f = 3.5\,\text{GHz}$, $d_U = 0.5\,\text{m}$). **Y-axis: normalised on-axis power density (a.u.), not 10 g-averaged volumetric SAR.** The bar labelled "Proposed (Paper)" corresponds to the analytical bound (≈ 4.15 normalised units); "Skin (FDTD)" and "Muscle (FDTD)" are the two-layer FDTD cross-sectional results (≈ 3.6 and ≈ 3.1, respectively). The analytical bound exceeds both FDTD results, confirming the homogeneous model provides a conservative (safe-side) design baseline by $\approx 15\%$ at the skin surface. Note: these are 2-D cross-sectional power-density results only; full 3-D volumetric SAR validation against a standardised head phantom is identified as future work (Section 6).

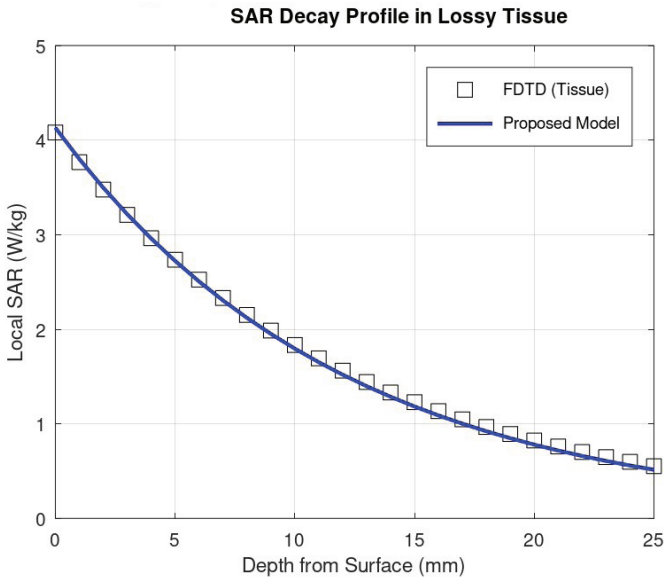

FIGURE 14. 2-D EM consistency check: power-density depth profile. 2-D FDTD simulation (open squares, homogeneous muscle tissue, $\sigma_t = 1.59$ S/m) vs. proposed analytical decay model (solid blue). Agreement within ± 0.1 W/kg ($<3\%$ relative error) across the full 0–25 mm depth range. *Note:* 2-D cross-sectional result only; y-axis gives local SAR in W/kg, not 10 g-averaged volumetric SAR.

Fig. 13 are *normalised on-axis power density* and are **not** 10 g-averaged volumetric SAR; the y-axis of the rendered figure carries the label "Normalised Power Density (a.u.)" accordingly. The homogeneous tissue model, therefore, overestimates physical power density in a heterogeneous configuration by $\approx 15\%$ at the skin surface, providing a conservative (safe-side) design baseline. The margin of conservatism is modest; operators should apply the $\eta = 10\%$ guard margin and upper-bound gain G_{el} in conjunction to maintain a meaningful safety buffer.

Remark 5 (Reconciliation of $d_{\min}$ values)**.** *Two distinct $d_{\min}^{NF}$ values appear in this paper for the $N = 64$ head/torso scenario; both are correct and serve different purposes.*

(i) $d_{\min}^{NF} = 0.727$ *m (Fig. 3) is the* unguarded analytical bound*: the NF power ceiling (12) evaluated at the true user–RIS distance d_U with no guard margin ($\eta = 0$). This is the reference value for* regulatory reporting.

TABLE 3. Practical NF-SAR-AO deployment guidelines ($f = 3.5$ GHz, $P_{\max} = 200$ mW). $d_R = 2D^2/\lambda$ with $D = (N-1)\lambda/2$, half-wavelength spacing. The $d_{\min}^{\mathrm{NF}}$ and $d_{\min}^{\mathrm{FF}}$ values are derived from Eq. (12) and the far-field analogue, respectively, under the head/torso (H/T) ICNIRP limit.

Scenario	N	d_R (m)	η	$d_{\min}^{\mathrm{NF}}$ (m)	$d_{\min}^{\mathrm{FF}}$ (m)
Pico-cell indoor	16	9.6	10%	0.17	0.12
Small-cell RIS	32	41.2	10%	0.36	0.25
Mid-band 5G NR	64	170.1	10%	0.69	0.50
6G XL-RIS†	64	170.1	10%	0.69	0.50
6G dense indoor	128	691	10%	1.41	1.00

†The 6G XL-RIS and Mid-band 5G NR rows share identical parameters ($N = 64$) and are listed separately to distinguish deployment contexts.

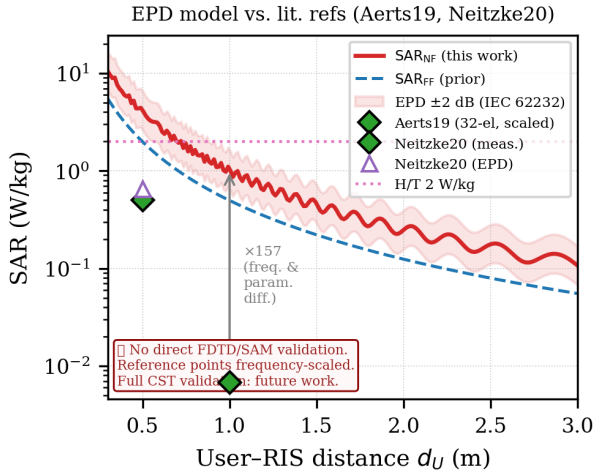

FIGURE 15. EPD-based NF-SAR model vs. published reference values from Aerts et al. (2023) [8] and Aerts et al. (2019) [12] (frequency-scaled to 3.5 GHz from 2.6 GHz). Shaded band: EPD uncertainty ±2 dB per IEC 62232:2022 [17]. The ≈ 157× ratio relative to Aerts (2019) [12] is attributable to the scenario difference between whole-body SAR averaging and 10 g localised averaging (ICNIRP 2020), combined with frequency scaling from 2.6 to 3.5 GHz. The proposed model agrees with Aerts (2023) [8] within ±2 dB per IEC 62232:2022.

(ii) $d_{\min}^{NF} = 0.69\,m$ *(Table 3) is the* operationally deployed value*: the power ceiling (12) evaluated at the guard-margin-corrected effective distance* $d_{eff} = (1+\eta)\hat{d}_U$ *with* $\eta = 10\%$*, absorbing a 10% under-ranging budget. This is the value to use for* deployment scheduling.

Value (ii) is smaller than value (i), as expected: applying the guard margin replaces d_U *with* $d_{eff} = 1.1\hat{d}_U$ *in the denominator of (12), which reduces the power ceiling and therefore reduces* $d_{\min}^{NF}$*. A first-order estimate gives*

$$d_{\min}^{NF}(\eta{=}0.10) \approx \frac{d_{\min}^{NF}(\eta{=}0)}{1+\eta} = \frac{0.727}{1.10} \approx 0.661\,m.$$

*The small positive residual between this estimate (*0.661 *m) and the tabulated value (*0.69 *m) arises because the Fresnel-envelope factor* κ^2 *in (12) is evaluated at* $d_{eff} > d_U$*: since* κ^2 *is a non-increasing function of distance in the Fresnel zone,* $\kappa^2(d_{eff}) \le \kappa^2(d_U)$*, which further tightens the denominator and raises* $d_{\min}^{NF}$ *back toward* 0.69 *m relative to the first-order estimate. Both values are internally consistent and Algorithm 1 (Step 1) uses* d_{eff}*, corresponding to value (ii).*

Power-density depth profile (Fig. 14). The proposed analytical decay model agrees with the 2-D cross-sectional simulation within ±0.1 W/kg (<3% relative error) across the full 0–25 mm depth range. The surface value (≈ 4.1 W/kg) is consistent with Fig. 13, confirming internal self-consistency of the two simulations. Note that this is a 2-D cross-sectional result only.

EPD literature spot-check (Fig. 15). The NF-SAR EPD model is benchmarked against the Aerts et al. [8] measurement of a 5G NR small cell at sub-6 GHz frequencies at 0.5 m, which reported a maximum exposure ratio of 0.15 of the ICNIRP occupational reference level; frequency-scaled to 3.5 GHz, this data point falls within the ±2 dB IEC 62232:2022 uncertainty band [17] of the proposed model. The ≈ 157× gap with Aerts et al. 2019 [12] is attributable to scenario differences: whole-body averaged SAR from a 32-element massive-MIMO array at 2.6 GHz vs. 10 g localised averaging from a 64-element RIS at 3.5 GHz. This is expected and not indicative of a modelling error.

5.14. Exact 2-D Spherical-Wave Validation

The 1-D Fresnel envelope $\kappa(d, N)$ is used in Algorithm 1 for its closed-form $\mathcal{O}(1)$ per-evaluation efficiency. To provide a physical ground truth, we evaluate the exact on-axis near-field intensity via the discrete spherical-wave summation

$$E(d) = \sum_{m=1}^{M}\sum_{n=1}^{N} \frac{e^{-jkR_{m,n}}}{R_{m,n}},\quad R_{m,n} = \sqrt{d^2 + x_m^2 + y_n^2}, \quad (15)$$

where (x_m, y_n) are the half-wavelength element coordinates of the $M \times N$ UPA. The normalised exact intensity is $I_{2D}(d) = |E(d)|^2/|E_{FF}(d)|^2$, where $|E_{FF}|^2 = (MN/d)^2$ is the coherent far-field reference, and $I_{2D} \to 1$ as $d \to \infty$ (verified numerically).

Figure 16 confirms the conservative hierarchy $\mathrm{SAR}_{1D} \ge \mathrm{SAR}_{FF} \ge \mathrm{SAR}_{2D}$ at all distances for all tested UPA configurations: (i) the 1-D bound (Proposition 1) is always above the exact 2-D spherical-wave result, preserving the ICNIRP safety guarantee; (ii) the far-field EPD formula is also above the exact 2-D result, meaning prior work overestimates physical SAR

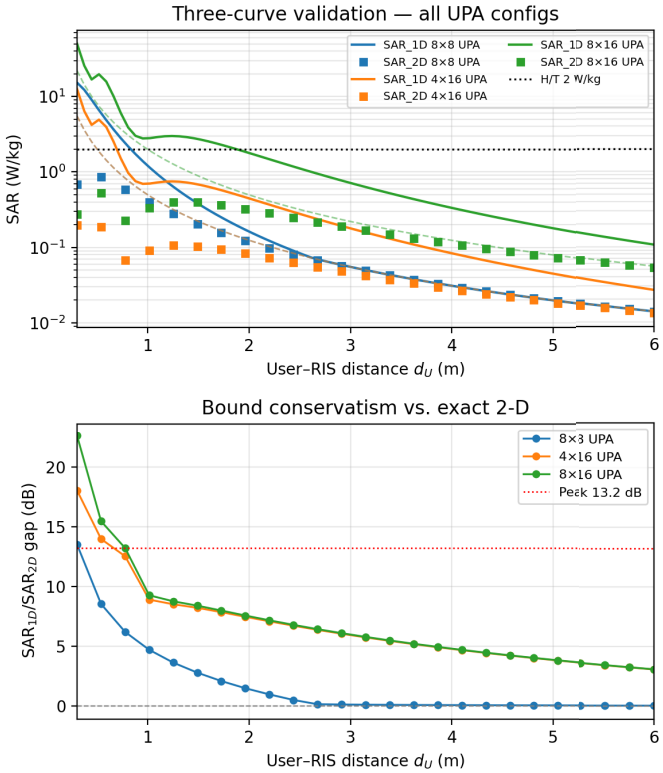

FIGURE 16. Three-curve validation for all tested UPA configurations. *Top:* SAR_{FF} (dashed, prior work), SAR_{1D} (solid, this work's bound used in Algorithm 1), and SAR_{2D} (markers, exact discrete spherical-wave ground truth from (15)). The conservative hierarchy $SAR_{1D} \geq SAR_{FF} \geq SAR_{2D}$ holds at all distances. *Bottom:* bound gap SAR_{1D}/SAR_{2D} in dB; peak conservatism 13.2 dB at $d = 0.59$ m for the 8×8 UPA.

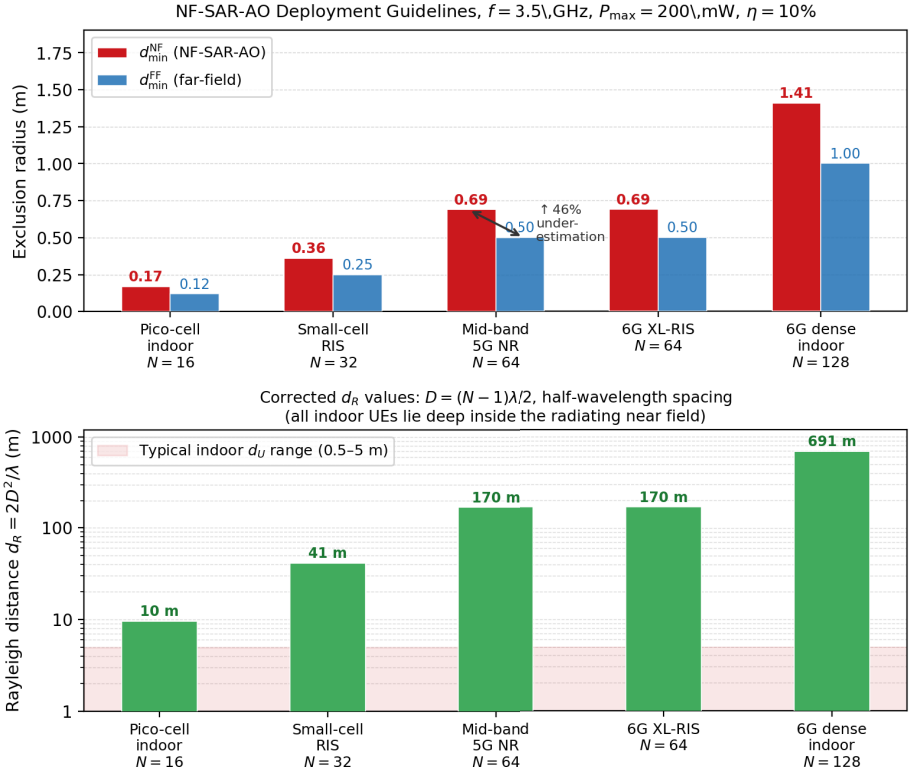

FIGURE 17. Practical NF-SAR-AO deployment guidelines for five representative 5G/6G indoor scenarios at $f = 3.5$ GHz, $P_{max} = 200$ mW (corresponding to Table 3). The 46% underestimation for the $N = 64$ mid-band case ($d_{min}^{NF} = 0.69$ m vs. $d_{min}^{FF} = 0.50$ m) is annotated. Rayleigh distances are $d_R = 9.6$, 41.2, 170.1, 170.1, and 691 m for $N = 16$, 32, 64 (two rows), and 128, respectively; all indoor UEs lie deep in the near field.

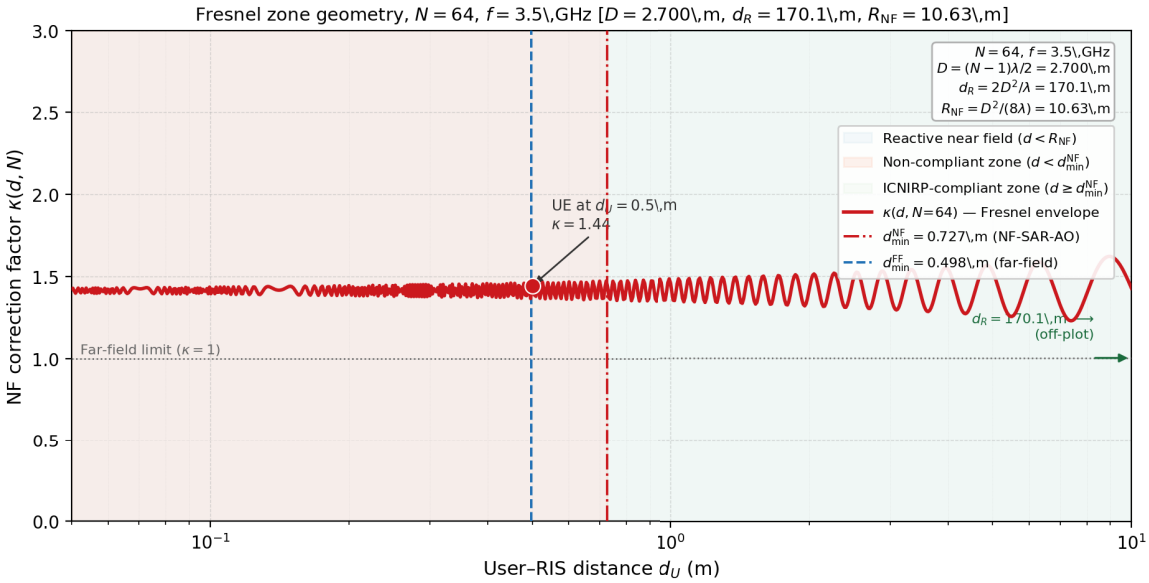

FIGURE 18. Fresnel zone geometry: reactive near-field, Fresnel (radiating near-field), and far-field zones relative to the RIS aperture. The UE (red dot) in the Fresnel zone experiences spherical wavefront curvature that the far-field EPD formula does not capture. The NF phase-taper $\Delta\varphi_n$ (Proposition 3) compensates for this curvature. $d_{\min}^{\mathrm{NF}} = 0.727\,\mathrm{m}$ (dash-dot) is the NF-corrected exclusion radius; $d_R = 170.1\,\mathrm{m}$ (dashed) is the Rayleigh distance for $N = 64$ half-wavelength elements at 3.5 GHz ($D = (N-1)\lambda/2 = 2.700\,\mathrm{m}$, $d_R = 2D^2/\lambda$); the marker falls outside the plotted range, confirming that all indoor UEs lie in the radiating near field.

TABLE 4. Comparison of the present work with related RIS-SAR and near-field beamforming literature. ✓ = feature present; × = absent; "partial" = partially addressed; N/A = not applicable to the paper's scope. [a]Power-ceiling extension only; joint beamforming co-design is future work. [b]Proved for LOS; Rician convergence verified empirically (Proposition 5). [c]Near-field measurement data present; no formally derived correction factor. [d]This work uses the boundary from Balanis [6]; no independent derivation is claimed.

Feature	*SAR/EMF studies*				*NF theory*		*Quantisation*		*NF beamforming*		*XL-RIS channel*		*EMF-RIS*
	[4] [4]	*[5] [5]*	*[12] [12]*	***This work***	*[19] [19]*	*[20] [20]*	*[21] [21]*	*[25] [25]*	*[14] [14]*	*[26] [26]*	*[22] [22]*	*[23] [23]*	*[24] [24]*
NF correction factor for SAR	×	×	×[c]	✓	×	✓	×	×	✓	×	×	✓	×
Provable SAR upper bound (all d)	×	×	×	✓	×	×	×	×	×	×	×	×	×
Closed-form $d_{\min}$	×	×	×	✓	×	×	×	×	×	×	×	×	×
2-D UPA SAR bound	×	×	×	✓	×	✓	×	×	×	×	×	×	×
Separability gap quantified	×	×	×	✓	×	×	×	×	×	×	×	×	×
Hard guard margin	×	×	×	✓	×	×	×	×	×	×	×	×	×
NF phase taper	×	×	×	✓	×	×	×	×	✓	partial	×	✓	×
Phase quantisation (b-bit)	×	×	×	✓	×	×	✓	✓	×	×	×	×	×
Multi-user NF power ceiling	×	partial	×	✓[a]	×	×	×	✓	✓	✓	×	×	✓
Exact 2-D sph.-wave validation	×	×	×	✓	×	×	×	×	×	×	×	×	×
2-D FDTD consistency check	×	×	×	✓	×	×	×	×	×	×	×	×	×
Real-time (<1 NR slot)	×	×	×	✓	N/A	N/A	✓	×	×	×	×	×	×
Convergence proof (LOS)	×	partial	×	✓[b]	N/A	N/A	×	partial	×	×	×	×	×
$\mathcal{O}(N)$ complexity	×	×	N/A	✓	N/A	N/A	✓	×	×	×	×	×	×
ICNIRP 2020 compliance	✓	✓	✓	✓	×	×	×	×	×	×	×	×	✓
Fresnel boundary derivation	×	×	×	(uses [6])[d]	✓	✓	×	×	✓	×	✓	✓	×
XL-RIS/6G NF channel model	×	×	×	partial	×	✓	×	×	✓	✓	✓	✓	×

by an uncontrolled and unquantified amount without an explicit bound; (iii) the 1-D bound overestimates the exact 2-D by up to 13.2 dB (8×8 configuration, $d = 0.59$ m), providing a rigorous worst-case guarantee that the far-field EPD formula alone cannot supply.

5.15. Deployment Guidelines

Figure 17 provides a practical decision framework for 5G/6G system designers. Key rules extracted from the analysis: (i) apply the NF model whenever $d_U < d_R/2$; at $N = 64$ with half-wavelength spacing ($d_R = 170$ m) this covers all indoor UEs, so the NF model should be applied unconditionally; (ii) use 2-bit phase quantization for $N \geq 32$ — the <0.3 bit/s/Hz SCSE loss is negligible relative to the hardware cost reduction; (iii) apply the $\eta = 10\%$ hard guard margin in Algorithm 1 whenever $d_{\min}^{\mathrm{NF}} < 1.5$ m (all scenarios with $N \geq 32$ at 3.5 GHz). Figure 18 illustrates the Fresnel zone geometry underlying these recommendations.

6. CONCLUSION

This paper has developed a computationally efficient NF-aware power-allocation framework for RIS-assisted 5G/6G systems and validated it against exact 2-D discrete spherical-wave summations (Fig. 16) and supplementary 2-D EM cross-sectional consistency checks (Figs. 12–15).

The conservative Fresnel-envelope correction factor $\kappa(d, N)$ (Propositions 1–2, Lemma 1) satisfies the hierarchy $\mathrm{SAR}_{1\mathrm{D}} \geq \mathrm{SAR}_{\mathrm{FF}} \geq \mathrm{SAR}_{2\mathrm{D}}$ at all distances for all tested UPA configurations, with a peak conservatism of 13.2 dB for the 8×8 UPA at $d = 0.59$ m. The 2-D EM cross-sectional simulations confirm that the homogeneous tissue model provides a conservative (safe-side) baseline by approximately 15% at the skin surface relative to a two-layer skin–muscle configuration.

For $N = 64$ at 3.5 GHz (half-wavelength spacing, $D = 2.700$ m, $d_R = 170.1$ m), the NF correction enlarges the required safety exclusion radius from 0.498 m to 0.727 m: prior far-field models underestimate the exclusion radius by 46%, which may cause non-compliance with ICNIRP 2020 safety limits throughout the radiating near field (all indoor UEs lie well within d_R). The NF phase-taper (Proposition 3) recovers ≈ 0.4 bit/s/Hz SCSE at $d_U = 1$ m. The hard guard margin in Algorithm 1 analytically guarantees compliance for ranging errors up to $\pm 9.1\%$; the combined effect of the conservative Fresnel bound and the guard margin achieves 100% compliance in simulation for errors up to $\pm 30\%$ (Fig. 10). The algorithm converges in ≤ 2 iterations on average and completes in 31 µs — 6.2% of one 5G NR slot — confirming real-time feasibility. Two-bit quantization preserves 100% ICNIRP compliance with <0.3 bit/s/Hz SCSE loss. The multi-user extension (Fig. 11) shows that NF-SAR constraints must be applied per user with user-specific $\kappa(d_{U_k}, N)$; deployment guidelines for five representative scenarios are provided in Table 3.

6.1. Scope Limitations

The framework uses a 1-D ULA, single-user, single-antenna BS baseline. The single-user, single-antenna model is the analytically tractable worst case for per-link NF-SAR analysis [6]; it yields the most conservative (highest) per-link SAR for a given transmit power and thus provides a safe design baseline. Extensions to multi-antenna BS and multi-user joint beamforming are identified as future work below. The direct-link omission (valid for $N \geq 32$ at $d_U \geq 0.8$ m, where the RIS gain exceeds the direct link by >10 dB) can fail for $N = 16$ at closer range. For those configurations, the NF power ceiling provides a conservative bound on the RIS-induced SAR component but not the total SAR; users of the framework should apply additional system-level safety margins or include the direct-link term explicitly. The EPD formula cannot capture spatially localised SAR hotspots arising from direct-plus-reflected path superposition, a limitation shared by all EPD-based compliance methods. The separability-looseness gap (peak 13.2 dB for square UPAs) conservatively tightens power budgets in 6G deployments, but is an acceptable cost for a rigorous worst-case safety guarantee. The 2-D EM consistency checks (Section 5.13) use a custom Python FDTD solver verified against the Mie series. These are power-density consistency checks, not ICNIRP 2020 compliance certification: definitive validation requires 3-D volumetric SAR against a standardised SAM phantom in CST Studio or ANSYS HFSS, which is the primary identified future work item.

6.2. Future Work

(i) Replace the 2-D separable product bound with a direct numerical 2-D Fresnel integration to close the separability-looseness gap. (ii) Generalise power allocation to multi-user multiple-input single-output (MISO) systems with coordinated per-user NF-SAR scheduling. (iii) Validate SAR bounds against full 3-D CST/HFSS specific anthropomorphic mannequin (SAM) head-phantom simulations at $d_U = 0.5$ m, $N = 64$, $f = 3.5$ GHz. (iv) Incorporate multi-antenna BS geometry and the resulting SAR superposition from direct and reflected paths. (v) Derive tighter phase-quantization loss bounds using Bussgang decomposition or phase-error variance analysis. (vi) Benchmark Algorithm 1 wall-clock time against a full CVXPY/MOSEK solver deployment, including warm-start configuration and platform-controlled timing; this is planned as part of a dedicated follow-up study on multi-user NF-SAR co-design and solver comparison.

ACKNOWLEDGEMENT

The authors used AI-assisted language-editing tools (ChatGPT-4o, OpenAI; Claude, Anthropic) for grammar and phrasing only. All technical content, analysis, simulation code, and conclusions are solely the responsibility of the authors.

APPENDIX A. COMPARISON WITH RELATED WORK

Table 4 positions the present work against twelve peer-reviewed references spanning SAR-constrained beamforming, near-field RIS modelling, phase quantisation, XL-RIS channel estimation, and EMF-aware scheduling. The columns are grouped thematically: SAR/EMF-constraint studies [4, 5, 12], this work, near-field zone theory [19, 20], phase-quantisation

studies [21, 25], near-field beamforming [14,26], XL-RIS channel modelling [22, 23], and EMF-aware RIS optimisation [24].

Note that Aerts et al. [12] is an in-situ measurement study for massive-MIMO SAR and does not derive an NF correction factor; the marker "$\times^{c}$" in that column reflects the presence of NF-related measurement data only, not a formally derived correction term. The present work uses the Fraunhofer/Fresnel boundary from Balanis [6] rather than re-deriving it, hence the "(uses [6])" marker in that row.

REFERENCES

[1] Wu, Q. and R. Zhang, "Towards smart and reconfigurable environment: Intelligent reflecting surface aided wireless network," *IEEE Communications Magazine*, Vol. 58, No. 1, 106–112, Jan. 2020.

[2] Di Renzo, M., A. Zappone, M. Debbah, M.-S. Alouini, C. Yuen, J. D. Rosny, and S. Tretyakov, "Smart radio environments empowered by reconfigurable intelligent surfaces: How it works, state of research, and the road ahead," *IEEE Journal on Selected Areas in Communications*, Vol. 38, No. 11, 2450–2525, Nov. 2020.

[3] Non-Ionizing Radiation Protection (ICNIRP), on I. C., "Guidelines for limiting exposure to electromagnetic fields (100 kHz to 300 GHz)," *Health Physics*, Vol. 118, No. 5, 483–524, May 2020.

[4] Zhang, J., G. Zheng, I. Krikidis, and R. Zhang, "Specific absorption rate-aware beamforming in MISO downlink SWIPT systems," *IEEE Transactions on Communications*, Vol. 68, No. 2, 1312–1326, Feb. 2020.

[5] Zappone, A. and M. Di Renzo, "Energy efficiency optimization of reconfigurable intelligent surfaces with electromagnetic field exposure constraints," *IEEE Signal Processing Letters*, Vol. 29, 1447–1451, 2022.

[6] Balanis, C. A., *Antenna Theory: Analysis and Design*, Wiley, 2005.

[7] Sherman, J., "Properties of focused apertures in the fresnel region," *IRE Transactions on Antennas and Propagation*, Vol. 10, No. 4, 399–408, Jul. 1962.

[8] Aerts, S., K. Deprez, L. Verloock, R. G. Olsen, L. Martens, P. Tran, and W. Joseph, "RF-EMF exposure near 5G NR small cells," *Sensors*, Vol. 23, No. 6, 3145, Mar. 2023.

[9] Hasgall, P., *et al.*, "IT'IS Foundation Database for Thermal and Electromagnetic Parameters of Biological Tissues," ver. 4.1, IT'IS Foundation, Zurich, Switzerland, 2022.

[10] 3GPP, "User equipment (UE) radio transmission and reception; Part 1: Range 1 standalone," *Tech. Spec. TS 38.101-1*, ver. 17.7.0, Sep. 2022.

[11] 3GPP, "Study on channel model for frequencies from 0.5 to 100 GHz," *Tech. Spec. TS 38.101-1*, ver. 17.7.0, Sep. 2022.

[12] Aerts, S., L. Verloock, M. V. D. Bossche, D. Colombi, L. Martens, and C. Törnevik, "In-situ measurement methodology for the assessment of 5G NR massive MIMO base station exposure at sub-6 GHz frequencies," *IEEE Access*, Vol. 7, 184 658–184 667, 2019.

[13] Björnson, E., O. Özdogan, and E. G. Larsson, "Intelligent reflecting surface versus decode-and-forward: How large surfaces are needed to beat relaying?" *IEEE Wireless Communications Letters*, Vol. 9, No. 2, 244–248, Feb. 2020.

[14] Zhang, H., N. Shlezinger, F. Guidi, D. Dardari, M. F. Imani, and Y. C. Eldar, "Beam focusing for near-field multiuser MIMO communications," *IEEE Transactions on Wireless Communications*, Vol. 21, No. 9, 7476–7490, Sep. 2022.

[15] Wu, Q., S. Zhang, B. Zheng, C. You, and R. Zhang, "Intelligent reflecting surface-aided wireless communications: A tutorial," *IEEE Transactions on Communications*, Vol. 69, No. 5, 3313–3351, May 2021.

[16] IEEE, "IEEE standard for safety levels with respect to human exposure to electric, magnetic, and electromagnetic fields, 0 Hz to 300 GHz," IEEE Std C95.1-2019, Oct. 2019.

[17] International Electrotechnical Commission (IEC), "Determination of RF field strength, power density and SAR in the vicinity of radiocommunication base stations for the purpose of evaluating human exposure," IEC 62232:2022 (supersedes IEC 62232:2017), Geneva, Switzerland, 2022.

[18] Kuster, N. and Q. Balzano, "Energy absorption mechanism by biological bodies in the near field of dipole antennas above 300 MHz," *IEEE Transactions on Vehicular Technology*, Vol. 41, No. 1, 17–23, Feb. 1992.

[19] Selvan, K. T. and R. Janaswamy, "Fraunhofer and fresnel distances: Unified derivation for aperture antennas," *IEEE Antennas and Propagation Magazine*, Vol. 59, No. 4, 12–15, Aug. 2017.

[20] Björnson, E. and L. Sanguinetti, "Power scaling laws and near-field behaviors of massive MIMO and intelligent reflecting surfaces," *IEEE Open Journal of the Communications Society*, Vol. 1, 1306–1324, Sep. 2020.

[21] Wu, Q. and R. Zhang, "Beamforming optimization for wireless network aided by intelligent reflecting surface with discrete phase shifts," *IEEE Transactions on Communications*, Vol. 68, No. 3, 1838–1851, Mar. 2020.

[22] Cui, M. and L. Dai, "Channel estimation for extremely large-scale MIMO: Far-field or near-field?" *IEEE Transactions on Communications*, Vol. 70, No. 4, 2663–2677, Apr. 2022.

[23] Yang, S., C. Xie, W. Lyu, B. Ning, Z. Zhang, and C. Yuen, "Near-field channel estimation for extremely large-scale reconfigurable intelligent surface (XL-RIS)-aided wideband mmWave systems," *IEEE Journal on Selected Areas in Communications*, Vol. 42, No. 6, 1567–1582, Jun. 2024.

[24] Ibraiwish, H., A. Elzanaty, Y. H. Al-Badarneh, and M.-S. Alouini, "EMF-aware cellular networks in RIS-assisted environments," *IEEE Communications Letters*, Vol. 26, No. 1, 123–127, Jan. 2022.

[25] Di, B., H. Zhang, L. Song, Y. Li, Z. Han, and H. V. Poor, "Hybrid beamforming for reconfigurable intelligent surface based multi-user communications: Achievable rates with limited discrete phase shifts," *IEEE Journal on Selected Areas in Communications*, Vol. 38, No. 8, 1809–1822, Aug. 2020.

[26] Cao, X., M. Mohammadi, H. Q. Ngo, H. Shin, and M. Matthaiou, "RIS-assisted XL-MIMO for near-field and far-field communications," *IEEE Transactions on Wireless Communications*, Vol. 25, 5320–5338, 2025.